Computational fluid dynamics analysis of bridge scour with a comparison of pier shapes and a debris fin

Tu, Xin L.; Gambaruto, Alberto M.; Newell, Richard; Pregnolato, Maria

DOI
10.1016/j.istruc.2024.106966

Publication date
2024

Document Version
Final published version

Published in
Structures

Citation (APA)
Tu, X. L., Gambaruto, A. M., Newell, R., & Pregnolato, M. (2024). Computational fluid dynamics analysis of bridge scour with a comparison of pier shapes and a debris fin. *Structures*, *67*, Article 106966. https://doi.org/10.1016/j.istruc.2024.106966

Structures 67 (2024) 106966

Contents lists available at ScienceDirect

Structures

journal homepage: www.elsevier.com/locate/structures

Computational fluid dynamics analysis of bridge scour with a comparison of pier shapes and a debris fin

Xin L. Tu [a], Alberto M. Gambaruto [b,*], Richard Newell [c], Maria Pregnolato [d,e]

[a] Department of Mechanical Engineering, University of Bristol, Bristol BS8 1TH, UK
[b] University of Bristol, School of Engineering Mathematics and Technology, Bristol, BS8 1TR, UK
[c] Network Rail, Milton Keynes, UK
[d] Delft Univ. of Technology, Dept. of Hydraulic Engineering, Delft 2628 CN, Netherlands
[e] University of Bristol, Dept. of Civil Engineering, Bristol, BS8 1TR, UK

ARTICLE INFO

Keywords:
Bridge scour
Debris fin
Computational fluid dynamics
Horseshoe vortex
Wall shear stress
Vorticity

ABSTRACT

The flow field near bridge piers is analysed using computational fluid dynamics (CFD) models to investigate bridge scour, which is one of the main safety concerns for bridges. Two indicators are used to characterise the scour hole, the horseshoe vortex (HV) core position relative to the bed, and the area of wall shear stress (WSS) above a sediment transport threshold of 1 Pa. The underlying fluid mechanics is detailed, establishing the relation between vorticity generation, the fluid strain rate and the WSS. The CFD models are validated against results in the literature, for the free surface around the pier and for the WSS at the bed. A parametric study with different pier widths, mass flow rates (MFR), and pier shapes is carried out, and these results are compared to an adapted pier with diverting fin inserted in the front. The adaptation shows that the diverting fin reduced the strength of the HV in front of the pier, and also reduces the total area of bed WSS above the threshold.

1. Introduction

Bridge scour is the erosion of the riverbed sediments around the base of the piers and is among the most common causes of bridge failure with high associated repair costs [1–3]. Local scour occurs when the sediments are removed substantially: a scour hole is formed and then evolves in depth, eventually exposing the foundation of the pier to the river flow. Local scour is associated to the presence of bridge piers and it plays a determining role in scour-related safety issues [4,5]. Severe scour holes undermine the stability of bridge piers, increasing the risk of bridge failure, especially during flooding [6]. Scour holes cause serious safety issues and financial losses, for example: bridge scour was found to be the cause of 23 bridge failures in the upper Mississippi basin in 1993, which incurred a loss of $15 million [1]; infrastructure failure in Georgia in 1994 due to scouring caused a damage of $130 million [1]; in 2015, scour also induced failure to the Lamington viaduct in Scotland [7] and indirect costs due to transport detours and delays attributed to a bridge failure in Cumbria [8,9]. In addition, climate change is causing more frequent and severe flooding events, which in turn are likely to exacerbate scour and hydrodynamic impact for bridges [10].

Various countermeasures exist to protect piers against scour. These methods are categorised into [4]: (i) passive countermeasures, if they reduce scour through a physical barrier, such as riprap (rock armour) or gabions; or (ii) active countermeasures, if they reduce scour through decreasing the strength of the downward flow and the horseshoe vortex, such as collars or slots. Moreover, the accumulation of floating debris is known to acerbate the effect of scour [6,11,12], by constraining the dividing streamline to be higher from the river bed and increasing the downwash. Consequently, several approaches are proposed to mitigate the accumulation of debris [13]. In particular, debris deflectors or fins can be installed on the upstream ends of piers and abutments, especially for areas of likely high flood flow velocities [14].

Extensive studies have been carried out to investigate local scours. It is apparent that the incoming flow forms a stagnation point on the front side of the bridge pier, effectively expressing a dividing streamline which separates the flow into an upward stream and a downward stream along the centre-plane section. The downward stream forms a horseshoe vortex (HV), which enables an elevated wall shear stress (WSS) on the riverbed [15]. Scouring is expected to initiate when the WSS of the river flow exceeds the critical shear stress of the riverbed

* Corresponding author.
E-mail addresses: xt16846@bristol.ac.uk (X.L. Tu), alberto.gambaruto@bristol.ac.uk (A.M. Gambaruto), richard.newell@networkrail.co.uk (R. Newell), m.pregnolato@tudelft.nl (M. Pregnolato).

https://doi.org/10.1016/j.istruc.2024.106966
Received 10 January 2024; Received in revised form 25 June 2024; Accepted 19 July 2024
Available online 25 July 2024

sediment in a localised region around the bridge pier. Field measurements and laboratory experiments have been conducted to characterise the scour formation based on the flow conditions described by the Reynolds number, the Froude number and the sediment diameter and type, among others [16–19]. Those dimensionless numbers lead to the formation of empirical formulae to predict scour depth that are widely used in industry [20,21].

Filed measurements are often challenging, and while laboratory experiments may accurately reproduce the real-world setting with few model assumptions, the use of *in silico* models such as computational fluid dynamics (CFD) allows for a detailed analysis of the flow fields around bridge piers. With the development of computational power and CFD packages, recent studies have established various simulation models to predict the scour depths based on dynamic mesh updating [22] and the turbulence structures around the bridge pier [23]. Various factors that affect the depth of the scour holes formed have been investigated both experimentally and computationally, including pier shapes [24,25] and the angle of the pier to the oncoming flow [26], with the computed CFD solution showing good agreement with experimental results. In addition to assessing scour depths and associated risks, mathematical modelling and CFD facilitate the investigation of effectiveness of pier adaptations for scour reduction. By comparison, the physical lab-based models are costly to run, especially when the parameters of the pier adaptations are yet to be explored. Consequently the current empirical formulae only consider generic pier shapes rather than adapted pier geometries.

This paper aims to show that the use of CFD and the detailed fluid mechanics analysis which is made possible, can complement the lab-based models and empirical formulae. The simulation models are cost-effective to run and are sensitive to parameter and geometry changes. Simple metrics such as the position of the HV core and area of riverbed above critical shear stress can be used to characterise the propensity for scour to occur, the scour depth and the extent of scour. The aim is achieved through three objectives:

1. to develop and validate a CFD model of the flow field around a single bridge pier using the finite volume solver Star-CCM+ [27] against existing experimental and computational results; and consequently develop simple measures to characterise the flow field based on the detailed CFD results;
2. to show that the position of the HV core and area of riverbed above critical shear stress can capture the change in parameters of the bridge pier and incoming flow in generic cases; and
3. to evaluate the effectiveness of pier adaptation, using a simple upstream fin design.

One of the primary factors of bridge failures is scour and practitioners are missing knowledge about its formation process and remedial interventions. Existing studies mostly reviewed scour equations and mechanism, as well as techniques for monitoring and countermeasures. However, more high resolution modelling and greater understanding of the underlying physics is needed to make significant breakthroughs, in order to devise pier adaptation methods which reduce the equilibrium scour depth and the extent of scour. This paper is innovatively combining a science- and engineering driven approach [4] by investigating the scour mechanism via CFD and countermeasure effectiveness of bridge scour respectively. The rest of the paper is organised as follows: Section 2 explains the fluid mechanics of the bridge scour process and the validation of the CFD models. Section 3 shows the results for generic cases, including varying the flow rate, different pier shapes, different pier diameters, and also a pier adaptation method of using a debris fin to mitigate scouring. Section 4 discusses the comparison of the generic cases with literature, and the evaluation of the debris fin. Section 5 summarises the main findings.

2. Methods

This paper adopts a CFD model for investigating the flow field around the bridge pier under different conditions. The analysis methods are based on the fluid mechanics around the bridge pier for scour initiation, which is used to characterise the scour hole by its depth and area. The standard computational model setup is shown in Fig. 1. Twelve cases are investigated, listed in Table 1 and which include: flumes 1–6 and 12 (circular pier, different pier width), flumes 7–8 (square pier, different rotation), flume 9 (elliptical), flume 10 (rectangular), flume 11 (adaptation).

2.1. Fluid mechanics

The water is assumed to be clear and free of debris, which can simply be modelled as an incompressible and Newtonian fluid. The governing equations for this problem are those of conservation of mass (continuity equation), and the conservation of linear momentum (Navier–Stokes equations), which are given by

$$\nabla \cdot \mathbf{u} = 0 \tag{1}$$

$$\frac{\partial \mathbf{u}}{\partial t} + (\boldsymbol{u} \cdot \nabla)\,\boldsymbol{u} = -\frac{1}{\rho}\nabla p + \nu \nabla^2 \boldsymbol{u} \tag{2}$$

where $\mathbf{u} = (u, v, w)^T$ are velocity components in $\mathbf{x} = (x, y, z)^T$ Cartesian directions respectively, p is the pressure, ρ is the density and ν is the kinematic viscosity.

When the incoming flow impinges on the bridge pier, the downward flow below the stagnation point creates a HV at the base of the pier. This HV is understood to be the main mechanism for scouring, as the rotational motion of the HV is able to mobilise the sediments and carry them downstream [28]. The stronger the HV, the greater the WSS it exerts at the riverbed, and the more sediment is carried away by the flow before reaching an equilibrium, and consequently the greater the equilibrium depth of scour.

Several nondimensional numbers have been investigated in relation to scour [16,17,19], and the two principal parameters which describe the physics regime are the Reynolds number and Froude number, while for piers exposed to waves it was found that the Keulegan–Carpenter number was of primary importance [18]. The Reynolds number is given by

$$Re = \frac{\rho V L}{\mu}, \tag{3}$$

where, assuming clear water conditions, $\rho = 997.56$ kg/m^3 and $\mu = 1.793 \times 10^{-3}$ Pa s being the density and dynamic viscosity of water. The characteristic length scale is denoted by L and the characteristic velocity is V. The Froude number is given by

$$\mathrm{Fr} = \frac{V}{\sqrt{gh}} \tag{4}$$

where g is the acceleration due to gravity and h is the water height.

2.1.1. Horseshoe vortex (HV)

There are several ways to measure the rotational motion of the flow. Vorticity is a vector denoted by, $\boldsymbol{\omega} = (\omega_x, \omega_y, \omega_z)^T$, which measures the rotation in the flow at a local point and is expressed as the curl of velocity field, hence

$$\nabla \times \boldsymbol{u} = \boldsymbol{\omega} = \left(\frac{\partial w}{\partial y} - \frac{\partial v}{\partial z}\right)\boldsymbol{i} + \left(\frac{\partial u}{\partial z} - \frac{\partial w}{\partial x}\right)\boldsymbol{j} + \left(\frac{\partial v}{\partial x} - \frac{\partial u}{\partial y}\right)\boldsymbol{k} \tag{5}$$

The higher the vorticity magnitude, the greater the rotational motion of an infinitesimal control volume. However, it is not straightforward to extract the maximum vorticity of the HV from simulation results directly, because vorticity is highest at the walls, with the shear rate magnitude equal to the vorticity magnitude. The shear rate magnitude is given by

$$\dot{\gamma} = \sqrt{\frac{1}{2}\left(\nabla \mathbf{u} + \nabla \mathbf{u}^T\right) : \left(\nabla \mathbf{u} + \nabla \mathbf{u}^T\right)} \tag{6}$$

Indeed, the *simple shear* strain which occurs at the walls due to the viscous stresses of the flow, generates an angular velocity which is equal to $\frac{1}{2}|\boldsymbol{\omega}|$.

In addition, the strength of the HV is related to its vertical position relative to the riverbed. The greater the distance of the vortex core from the river bed or from the pier leading edge, suggests that the downward flow has a greater mass flow rate and higher angular momentum when it approaches the riverbed. Therefore, the comparison of the position of the HV core is related to the change in the equilibrium scour depth in parametric studies. It is an alternative measure than comparing the maximum magnitude of WSS, especially as the latter is a point measurement taken at a mesh node and is hence sensitive to local effects and noise or artefacts.

Finding the height of the HV core from the river bed first requires a definition of the vortex core, for which the Q criterion ($Q > 0$) [29] and λ_2 criterion ($\lambda_2 < 0$) [30] are commonly used. λ_2 is the second eigenvalue of $S^2 + \Omega^2$, where S and Ω are the symmetric and anti-symmetric components of the strain rate tensor (the velocity gradient tensor), respectively. A vortex is then defined as the volume in which $\lambda_2 < 0$ [30], which was found to be more expressive for a variety of example cases, compared to other vortex identification methods. This criterion is derived by neglecting the unsteady irrotational straining and viscous effects, and effectively identifies the local pressure minimum in a plane section. In the problem cases considered in the present study (see Table 1), the forces due to viscosity are low in comparison to inertial forces since the Reynolds number is high ($Re \approx 2 \times 10^5$). Additionally, the flow field is modelled as quasi-steady, since the boundary conditions are constant and the flow field is largely steady except for the turbulent wake which are inherently unsteady. Low Strouhal number oscillatory behaviour of horseshoe vortex systems has been reported in [17,18]. Coherent structures in turbulent wakes have nonetheless also been successfully identified using the λ_2 criterion [31]. For the problem cases investigated, thresholding the λ_2 criterion to $\lambda_2 < -50$ helps filter out small wake vortices that are not of interest. The vertical position of the HV is calculated as the closest distance from the river bed to the iso-surface of $\lambda_2 = -50$. The upstream distance from the pier leading edge is also computed in this fashion. It should be noted that for Flume 11 (fin adaptation, see Table 1) the upstream distance to the HV is carried out at 20° to the upstream direction as the HV is inhibited by the fin and is only formed at an angle before extending downstream.

2.1.2. Wall shear stress

On the basis that scour initiates when WSS is greater than the critical shear stress, the threshold WSS value can indicate an estimate of the scour area. The critical shear stress for incipient sediment motion, τ_0, can be obtained from a widely used empirical model utilising the Shields Diagram [32], which relates a dimensionless critical shear stress parameter, τ^*, to the Reynolds number of the sediment, Re_s, which can be obtained from Eq. (3), with the characteristic length $L = d_s$ representing the mean sediment diameter, d_s. Taking $d_s = 1.07$ mm [33], then $Re_s = 600$, and $\tau^* = 0.06$ is subsequently obtained from the Shields curve. Finally, the critical shear stress is given by

$$\tau_0 = \tau^*(\gamma_s - \gamma)d_s \tag{7}$$

where γ_s is the mean sediment specific weight and γ is the specific weight of water [32]. Setting $\gamma_s = 26.4$ kN/m^3 from [33], then Eq. (7) yields $\tau_0 = 1.0$ Pa. The value of d_s may range between 0.84 mm and 1.07 mm, setting the investigation in the clear water scour regime, whereas smaller d_s (for example 0.46 mm) falls in live bed scour regime [33]. The largest particle Reynolds number is consequently observed in the clear water regime, while the critical shear stress will be smaller in the live bed scour regime. The area of the river bed where $\tau > 1$ Pa is recorded, being where scour is highly expected to occur, and serves to compare the extent of the scour in the sequence of parametric studies carried out.

On the flume bed, given that the fluid is modelled as incompressible and Newtonian, the WSS is given by

$$\boldsymbol{\tau}_{bed} = \mu\ \hat{\boldsymbol{n}} \cdot \left(\nabla \boldsymbol{u} + \nabla \boldsymbol{u}^T\right) \tag{8}$$

where $\hat{\boldsymbol{n}}$ is the inwards facing unit normal vector to the flume bed (at $y = 0$ m). The deviatoric stress tensor, which accounts for viscous stresses in the flow, is given by $\mathbf{t} = \mu\left(\nabla \mathbf{u} + \nabla \mathbf{u}^T\right)$. For the setup shown in Fig. 1, where $\hat{\boldsymbol{n}} = (0, 1, 0)^T$, then bed WSS can be written simply as $\boldsymbol{\tau}_{bed} = \mu\ (\partial u/\partial y, 0, \partial w/\partial y)^T$, which is tangential to the wall as expected since an incompressible and Newtonian fluid has no normal viscous forces.

2.2. Relationship between wall shear stress and vorticity

The wall shear stress is the tangential fluid traction on the wall surface effected by viscosity and relates to the vorticity on the wall as [34]

$$\boldsymbol{\tau}_{bed} = \hat{\boldsymbol{n}} \cdot \mathbf{t} = -\mu\ \hat{\boldsymbol{n}} \times \boldsymbol{\omega} \tag{9}$$

For the setup presented in Fig. 1, where the stationary wall of the bed lies in the $x - z$ plane, we can readily verify this by simplifying the vorticity given by Eq. (5) to obtain $\boldsymbol{\omega}|_{\text{wall}} = (\partial w/\partial y, 0, -\partial u/\partial y)^T$. Indeed the magnitude of the wall shear stress and the vorticity fields differs only by a scaling factor which is the dynamics viscosity, while these two vector fields are orthogonal on the wall [35]. Given that the occurrence of scour can be assumed to be related to a threshold value of wall shear stress magnitude, then it is appropriate to investigate the vorticity field and the horseshoe vortex in relation to the risk to scour.

The vorticity is understood as the curl of the velocity field (Eq. (5)), while its behaviour may alternatively be described as a consequence of the vorticity transport equation, given by

$$\frac{\partial \boldsymbol{\omega}}{\partial t} + (\mathbf{u} \cdot \nabla)\boldsymbol{\omega} = (\boldsymbol{\omega} \cdot \nabla)\mathbf{u} + \nu \nabla^2 \boldsymbol{\omega} \tag{10}$$

where ν is the kinematic viscosity. The term $(\mathbf{u} \cdot \nabla)\boldsymbol{\omega}$ expresses the advection of vorticity, $(\boldsymbol{\omega} \cdot \nabla)\mathbf{u}$ is responsible for vortex stretching and tilting, and $\nu \nabla^2 \boldsymbol{\omega}$ describes the diffusion of vorticity. Vorticity is a conserved property, such that

$$\nabla \cdot \boldsymbol{\omega} = \mathbf{0} \tag{11}$$

Considering the fluid mechanics on the flume bed in detail, assuming a no-slip condition such that the flow has zero velocity since, then the vorticity transport equation reduces to a diffusion type equation i.e.

$$\frac{\partial \boldsymbol{\omega}}{\partial t} = \nu\ \nabla^2 \boldsymbol{\omega} \tag{12}$$

Rewriting the right hand side as $\nu \nabla^2 \boldsymbol{\omega} = \nu \nabla \cdot (\nabla \boldsymbol{\omega})$ we can understand the flux of vorticity into the flow as

$$\sigma = \nu\ \frac{\partial \boldsymbol{\omega}}{\partial \hat{\boldsymbol{n}}} = \nu\ \hat{\boldsymbol{n}} \cdot \nabla \boldsymbol{\omega} \tag{13}$$

Hence, the amount of vorticity entering the flow is not directly related to the vorticity on the wall (hence the WSS), but rather the gradient of vorticity in the normal direction. One can also readily observe that the wall-normal component of vorticity (ω_y in our case) is zero, though the gradient is non-zero.

Given the present setup with the stationary wall lying in the $x - z$ plane, and using Eqs. (11) and (2), the flux of vorticity into the flow (Eq. (13)) can be written explicitly for each term by

$$\nu \frac{\partial \omega_x}{\partial y} = \nu \frac{\partial}{\partial y}\left(\frac{\partial w}{\partial y} - \frac{\partial v}{\partial z}\right) = \nu \frac{\partial^2 w}{\partial y^2} = \nu \nabla^2 w = \frac{1}{\rho}\frac{\partial p}{\partial z} \tag{14}$$

$$\frac{\partial \omega_y}{\partial y} = -\left(\frac{\partial \omega_x}{\partial x} + \frac{\partial \omega_z}{\partial z}\right) \tag{15}$$

$$\nu \frac{\partial \omega_z}{\partial y} = \nu \frac{\partial}{\partial y}\left(\frac{\partial v}{\partial x} - \frac{\partial u}{\partial y}\right) = -\nu \frac{\partial^2 u}{\partial y^2} = -\nu \nabla^2 u = -\frac{1}{\rho}\frac{\partial p}{\partial x} \tag{16}$$

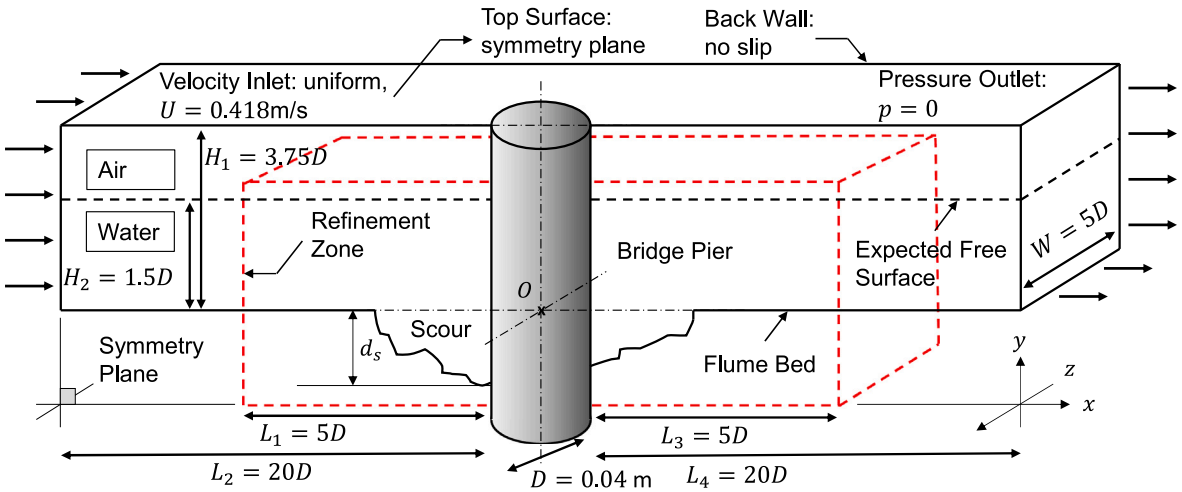

Fig. 1. Visualisation of the computational domain. Dimensions and boundary conditions are specified.

Following [36], this may be rewritten more succinctly as

$$(\nabla \times \boldsymbol{\omega}) \cdot \boldsymbol{s} = -\nabla^2 \boldsymbol{u} \cdot \boldsymbol{s} = \frac{1}{\nu} \frac{\partial p}{\partial \boldsymbol{s}} \tag{17}$$

for any surface tangent vectors **s**.

These relations imply that the vorticity fluxes can be measured by pressure gradients, and are due to the viscous traction at the wall. Once the vorticity has been generated at the wall, we see from Eq. (10) that vorticity is advected and diffused in the flow, as well as undergoing stretching and tilting which if positive increase the vorticity.

The presence of the HV in proximity to the river bed is predominantly the result of the vorticity produced: (i) along the river bed, and (ii) along the pier as the flow is directed downwards below the dividing streamline. Since the magnitude of vorticity and wall shear stress are proportional, both vector fields are linked by physical principles, and the analysis of the HV can be employed to infer the propensity and severity of scour. Furthermore, the flux of vorticity is related to the pressure gradient along the wall, which can be understood as tangential acceleration of the flow along the bed, and it is relevant to investigate this phenomenon.

2.3. CFD model and setup

The CFD package Star-CCM+ was used for simulations, which employs the Finite Volume Method (FVM) to discretise the spatial domain. A representative drawing of the computational domain is shown in Fig. 1. The flume geometry is symmetrical about the centreline, so a symmetry plane boundary condition is used to reduce the computational cost. However, with this procedure any asymmetry in the wake, such as the dynamics of vortex shedding behind the pier or the flow within the separated wake [17,18,37,38], will not be well represented. The domain has a uniform velocity inlet and pressure outlet (zero pressure) boundary conditions, with the bulk flow direction in the positive x-axis (from left to right in all figures shown). A scour bed geometry was taken from [33] for a validation case, while a flat bed was simulated for other cases. The top surface is set to a symmetry boundary condition, and the back wall is set to a no-slip boundary condition. The inlet velocities, pier parameters (pier shape and pier width, D), and the flume dimensions of the models vary between cases for validation against different experimental data sets and the parametric studies. Approximately, the dimension of the flume was set as $20D$ upstream and $20D$ downstream in the x-axis, to allow the flow to fully develop, and the flume width is $10D$, hence with $5D$ on either side of the pier in the z-axis, so that the boundary has little effect on the region near the pier. The Volume of Fluid (VoF) method is used to simulate the water and air interface, allowing turbulent energy to dissipate through the free surface.

A Reynolds-Averaged Navier–Stokes (RANS) model is used to simulate the turbulent flow around the bridge pier. RANS models usually employ two equations to approximate small scale turbulent interactions, with one solving for the turbulent kinetic energy, k, and the other solving for the rate of dissipation of turbulent energy, ϵ (the $k-\epsilon$ model), or the specific rate of dissipation, ω (the $k-\omega$ model). The free surface profiles of the river flow along the mid-plane section ($z = 0$) using both these RANS models are compared with literature to identify the more appropriate turbulence model. As presented in the results, it is found that the $k-\omega$ model is seen to be more suitable for the current study and is employed for all cases investigated.

The segregated, implicit unsteady solver was used, which employs the SIMPLE scheme. The simulation was run for the duration of 10 advection time units, defined here as the time taken for the bulk flow to transit from inflow to outflow of the computational domain. The residuals of the solver are kept below 10^{-8} throughout. The mesh consists of trimmed cells, and has a local refinement around the bridge pier, with refined element size of $\delta x = 0.0025$ m. The time step is adaptive and based on the Courant–Friedrichs–Lewy (CFL) number on the free surface, and was constrained to ≤ 0.1.

A mesh independence study was carried out for the baseline simulation, Flume 2 (see Section 2.4), employing discretisation sizes of 3.2 mm, 3 mm, 2.5 mm and 1.6 mm in the region of interest around the pier (±12.5D upstream and downstream), resulting in mesh cell counts of 0.96M, 1.24M, 5.03M, and 9.6M elements, respectively. The recorded computational time for running Flume 2 was 192 7440 s, which translates to ∼33.4 h on a 16-core 2.6 GHz workstation.

2.4. Problem cases investigated

A number of cases are considered in the present study, firstly to validate the computational models and the setup used, secondly to carry out a sequence of parametric studies, and finally to investigate the effects of a pier adaptation on bridge scour and compare to the previous results. Table 1 summarises the flume set up for the validation cases, the parametric studies, and the adapted pier model, all in which the bed is flat.

2.4.1. CFD model and setup validation (Flume 2 and Flume 12)

The validation of the computational model and solver settings is twofold. Firstly, the benchmarking related to the water-air interface, also known as the free-surface, is carried out. This interface surface changes and adapts in shape as the flow encounters the pier, and allows

Table 1
List of simulations and flow field characteristics for some of the validation studies (Flume 2 and Flume 12), parametric study (Flume 1–10) and investigation into debris fin pier adaptation (Flume 11).

Problem Case #	Pier shape	Pier width (D) (m)	Mass flow rate (kg/s)	Flow depth (m)	Velocity at inlet (m/s)	Fr	Re_p $\times 10^4$	HV core position (x, y) (m, m)	Area of bed with WSS > 1 Pa ($\times 10^{-4}$ m^2)
Flume 1	Circular	0.030	10	0.060	0.418	0.545	1.96	(−0.0096,0.0028)	64.7
Flume 2	Circular	0.040	10	0.060	0.418	0.545	2.62	(−0.0161,0.0033)	253
Flume 3	Circular	0.050	10	0.060	0.418	0.545	3.27	(−0.0216,0.0040)	375
Flume 4	Circular	0.040	5	0.040	0.313	0.499	1.96	(−0.0153,0.0033)	21.2
Flume 5	Circular	0.040	15	0.075	0.500	0.583	3.13	(−0.0138,0.0035)	469
Flume 6	Circular	0.040	20	0.090	0.556	0.591	3.48	(−0.0126,0.0038)	584
Flume 7	Square	0.040	10	0.060	0.418	0.545	3.33	(−0.0227,0.0053)	419
Flume 8	Square (45°)	0.040	10	0.060	0.418	0.545	2.36	(−0.0018,0.0031)	297
Flume 9	Elliptical	0.040	10	0.060	0.418	0.545	4.14	(−0.0034,0.0032)	281
Flume 10	Rectangular	0.040	10	0.060	0.418	0.545	5.00	(−0.0234,0.0054)	419
Flume 11	Debris fin	0.040	10	0.060	0.418	0.545	7.62[b]	(−0.0062, 0.00803)[a]	188
Flume 12	Circular	0.067	10.9	0.050	0.330	0.465	3.41	(−0.0353,0.0053)	152

[a] The vortex core was extracted at 20° to the symmetry plane at the junction of the two vortices coming from the fin.

[b] Re_p at the bottom of the pier including the length of fin: Eq. (3) may be used to compute Re_p, with an equivalent hydraulic diameter to set the characteristic length $L = (0.5\pi D + 2L_5)$, hence $\frac{1}{2} \times$ pier perimeter $+ 2 \times$ fin length at base. See Fig. 3 for definition of fin dimensions.

Table 2
A comparison of the turbulence models used in this study and that of [23].

Model	CFD software	Turbulence model	Cell size (l × w × h) [m]	Time Discretisation
Ducrocq 1	OpenFOAM	RNG $k-\epsilon$	(0.0001–0.05) × (0.0001–0.02) × 0.001	CFL < 1
Ducrocq 2	OpenFOAM	$k-\omega$ SST	(0.0001–0.05) × (0.0001–0.02) × 0.001	CFL < 1
Model 1	STAR-CCM+	$k-\omega$ SST	(0.0025–0.005) × (0.0025–0.01) × (0.0025–0.005)	CFL < 0.1
Model 2	STAR-CCM+	$k-\epsilon$	(0.0025–0.005) × (0.0025–0.01) × (0.0025–0.005)	CFL < 0.1

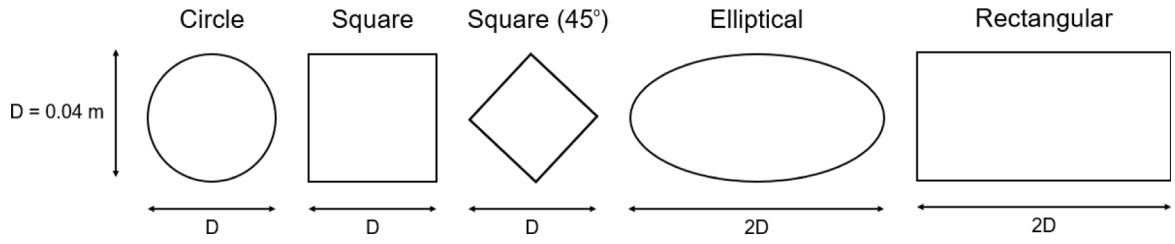

Fig. 2. Pier shapes investigated, as reported in Table 1. The pier width is kept the same for these cases, as the flow direction is from left to right in simulations.

energy to dissipate through the interface. The validation for this aspect is carried out by comparison with the results using the OpenFOAM software package and experimental results, from recent literature [23]. For this validation study, identified as Flume 2 in Table 1, the inlet velocity is 0.418 m/s, the pier diameter is 0.04 m and the upstream flow depth is 0.06 m. The comparison of the computational model solver settings is shown in Table 2, where both the $k-\omega$ SST and $k-\epsilon$ RANS turbulence models were tested.

Secondly, the benchmarking related to the bed wall shear stress is carried out, by means of a comparison to the simulation results presented in [33]. The setup involves a pier diameter of 0.067 m, the inlet velocity is 0.33 m/s and the upstream flow depth is 0.05 m. The flow field is simulated at different stages of scour. The flume bed is assumed to be rigid, and the topology at various stages of scour are reproduced from [33], at times $t = 0, 5, 60$ and 150 min, to represent the initial flat bed, intermediate stages of scour and the equilibrium scour topography. Previous studies showed that for model scale experiments, rapid scour occurs within the first two hours, and afterwards the scour depth tends asymptotically to the equilibrium scour depth [39]. In Table 1, the problem case Flume 12 corresponds to the $t = 0$ case (flat bed).

2.4.2. Parametric study of pier shape and flow conditions (Flume 1–10)

A parametric study is carried out on several parameters that affect the flow field around the pier, namely, the pier width, the pier shape and the flow rate, which also influences the flow depth. The effect of changes in parameters on the maximum scour depth have already been considered in the literature, by means of numerical modelling and laboratory experiments [24–26,40], however only a few have discussed the characteristics of the flow field which is the cause for the change in the maximum scour depth. The parametric study carried out additionally serves as a comparison data set for the pier adaptation investigated.

The effect of altering the pier width is compared between Flume 1–3, while Flume 2, 4–6 compare the effect of different flow rates, and finally Flume 2, 7–10 involve different pier shapes as shown in Fig. 2. The setup for Flume 2 therefore acts as overall baseline for the changes in parameters. The rectangular pier (Flume 10) has a doubled length in the flow direction as compared to the square pier (Flume 2). The square (45°) pier (Flume 8) is a square pier rotated with the corner facing into the flow, however it has a smaller cross-sectional area than the square pier (Flume 2) in order to keep the pier width the same, hence a constant Reynolds number to ensure that the physics regime of the flow is unchanged.

2.4.3. Pier adaptation (Flume 11)

Pier adaptation is modelled in Flume 11 and consists in a debris fin, which seeks to divert the oncoming flow at the pier to avoid debris accumulation, with the design inspired from existing constructions [14]. A thin, trapezoidal fin was fitted in front of the pier, with the dimensions shown in Fig. 3, otherwise employing the same shape and flow specifications as the baseline pier setup (Flume 2). For simplicity, the bottom length L_5 is chosen to be the same as the flow depth, hence $H_2 = 0.06$ m. The top length L_6 is introduced to avoid sharp edges,

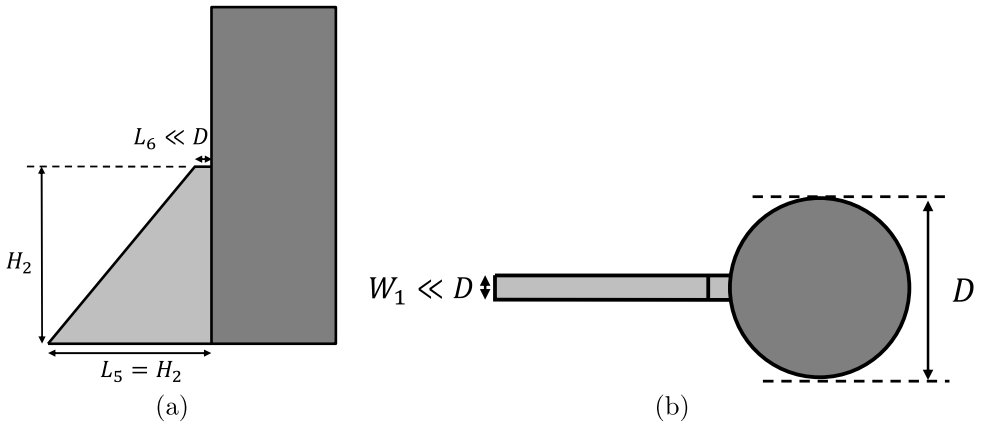

Fig. 3. Schematic of the pier adaptation design as a debris fin to reduce equilibrium scour depth: (a) front view; (b) top view.

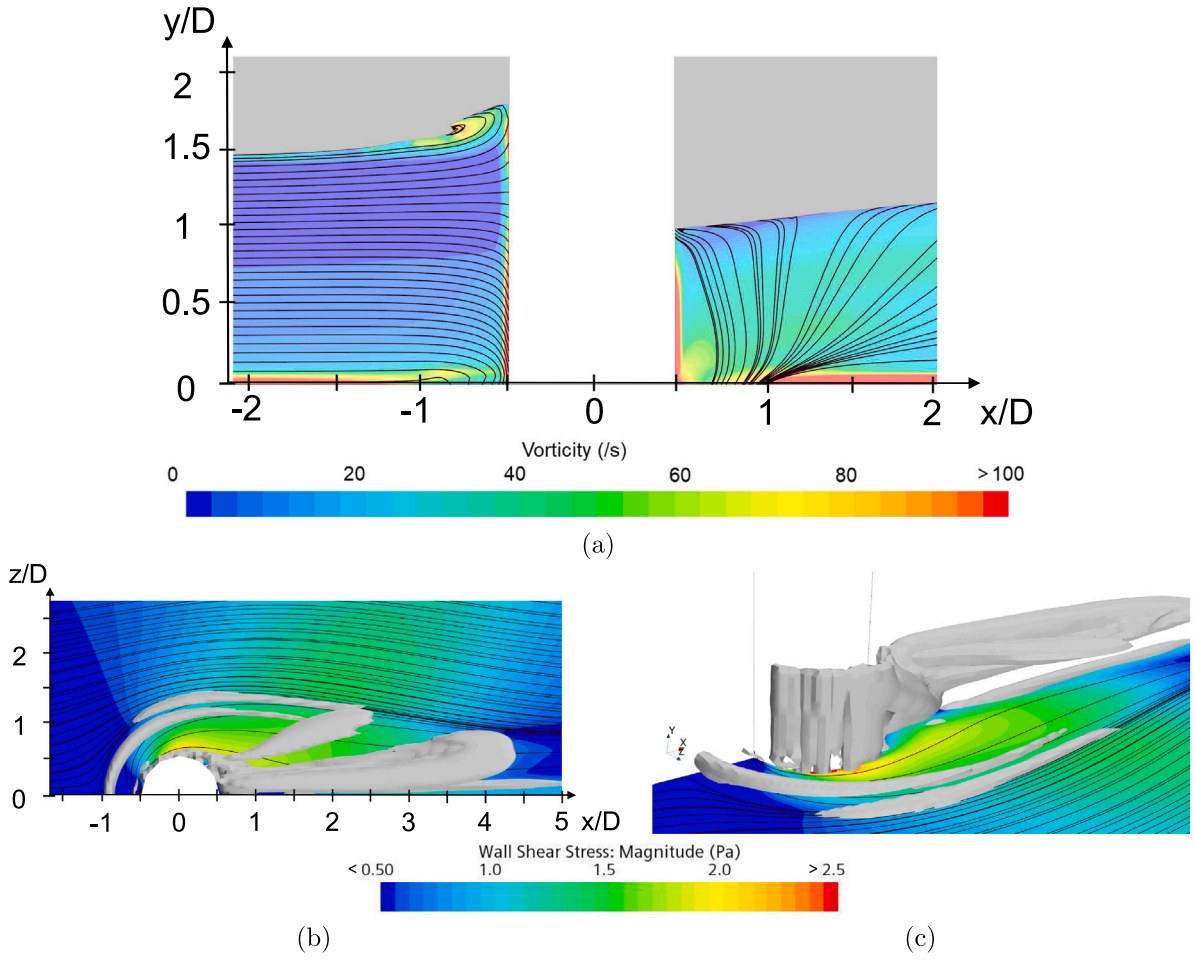

Fig. 4. Results for Flume 2. (a) Map of vorticity magnitude with streamlines on the symmetry plane (z/D = 0), hence along the centre of the flume. The blank (white) space indicates the presence of a pier. The grey area is that of the air above the water. Immediately downstream of the pier, streamlines are not present as this is a separated flow region. (b) Top view and (c) perspective view of surface shear lines on the flume bed, with vortex structures identified by the grey surfaces. The surface shear lines are obtained from integrating the wall shear stress along the flume bed. Flow direction is from left to right.

and is arbitrarily chosen to be 0.15 D. The thickness of the fin, W_1, was also arbitrarily chosen to be 0.05 D, though this would depend on the strength of the material used in real life scenarios. This design is intended to be representative and simple, being approximately a right angle isosceles triangle, and no attempt was made to optimise it. The arbitrarily chosen dimensions of the top length (L_6) and fin width (W_1) were intended to be small compared to the pier width, and the resulting flow field is not foreseen to be sensitive to modest changes in these dimensions.

3. Results

It is worth taking a closer look at the fluid dynamics for Flume 2 in order to highlight key features common to this type of problem. A plane

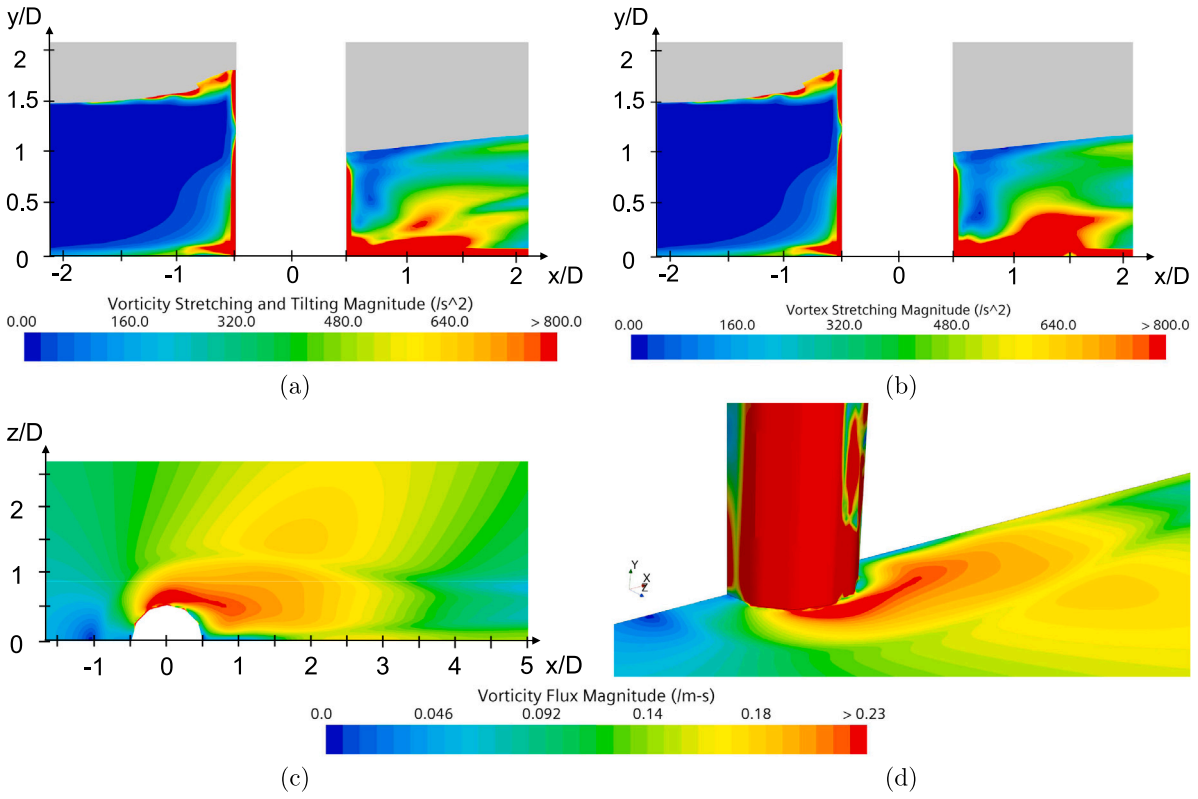

Fig. 5. Results for Flume 2. Cross-section on channel symmetry plane (z/D = 0) showing: (a) vorticity stretching and tilting magnitude (L_2-norm) given by $|(\boldsymbol{\omega}\cdot\nabla)\boldsymbol{u}|$; (b) magnitude of direct strain of vorticity given by $\sqrt{\left(\omega_x\frac{\partial u}{\partial x}\right)^2+\left(\omega_y\frac{\partial v}{\partial y}\right)^2+\left(\omega_z\frac{\partial w}{\partial z}\right)^2}$. (c) Cross-section on flume bed (y/D = 0) and (d) perspective view, showing boundary vorticity flux magnitude (L_2-norm) given by $|\nu\,\hat{\boldsymbol{n}}\cdot\nabla\boldsymbol{\omega}|$. Flow direction is from left to right.

section along the centre of Flume 2 is presented in Fig. 4, coloured by vorticity magnitude and showing streamlines, which were seeded at the inflow section on the symmetry plane. In this figure a dividing streamline is discernible by being approximately perpendicular to the pier wall as it impinges, enabling the stagnation point on the pier to be identified. The upward stream rotates in opposite direction to the downward stream. The former creates a change in the free surface, and the latter forms a HV at the pier base, whose vortex core is readily identifiable. Along the front half of the pier, the roll-up of the HV induces upstream flow along the river bed, which causes the flow to separate on the bed, and indeed we also observe that the WSS drops upstream of the HV. The vorticity magnitude is seen to be high at the vortex core as well as the walls (pier surface and flume bed), though principally in regions where the flow is approximately parallel to the wall. The streamlines do not appear in the immediate downstream wake region around the pier, as this is a separation bubble, while further downstream the streamlines return to the centre plane, first reappearing in proximity of the flume bed indicating the separation bubble is smallest closer to the flume bed, as expected. The flume bed and the pier surface are modelled as smooth, though in many cases they exhibit some rugosity, for example along the river bed, or due to pier brick work or rock armour and aprons used in scour prevention. This rugosity will promote unsteadiness and mixing, leading to higher velocity gradients and hence higher vorticity generation at these solid boundaries. Additionally, since these boundary layers have higher momentum, they lead to delayed flow separation around bluff bodies (such as piers) and hence also reduce the extent of flow separation and recirculation regions to the side and downstream of the pier. Overall, we would expect rugosity to increase the propensity for scour.

It is apparent from the WSS map and the vortices identified, shown in Fig. 4, that while there is a palpable correlation between the high WSS regions and the HV, the precise inference is not immediately clear. However, a closer correspondence is found when considering the magnitude of boundary vorticity flux, as shown in Fig. 5. From this figure we see that the generation of vorticity is closely related to the regions where WSS is high and susceptible to scouring, and this generated vorticity of the bed is convected and diffused into the free stream to form the HV, while a cascade of smaller vortices is also present [17,34]. The magnitude of the vorticity stretching and tilting, as well as magnitude of the direct strain of vorticity, are both shown in Fig. 5 and are related to an increase of vorticity when analysed locally. Regions of high vorticity strain appear on the free surface and where the HV is located, while there is a dip at the location of the stagnation point on the pier. In the wake region, the vorticity strain is generally directed up and away from the bed, due to the vortex structures formed in the wake of the pier. In line with the results reported in [17], multiple HV systems are present.

These results are related to a flat bed setup, hence the initiation of scour, which appears to be located predominantly laterally round the pier. The flat bed configuration appears as an unstable equilibrium, and the abrasive nature of the accelerating flow as it flows round the pier, together with the upwards flow (*upwash*) induced by the HV, enables scour to develop. The further development and propagation of scour can be envisioned to be a cascade effect. As the scour depth increases, the HV sits lower in the newly formed depression, such that the lip of the scour boundary is subjected to an upwash flow from the HV facilitating resuspension and entrainment of sediment at the scour lip, thus shifting the sediment and enabling scour progression. Scour can hence progress from the pier lateral locations easily, by resuspending sediment along the scour lip, and progressing further. Further scouring mechanisms are envisioned at deeper scour depths, which cannot be inferred with confidence from the simulations of a flat

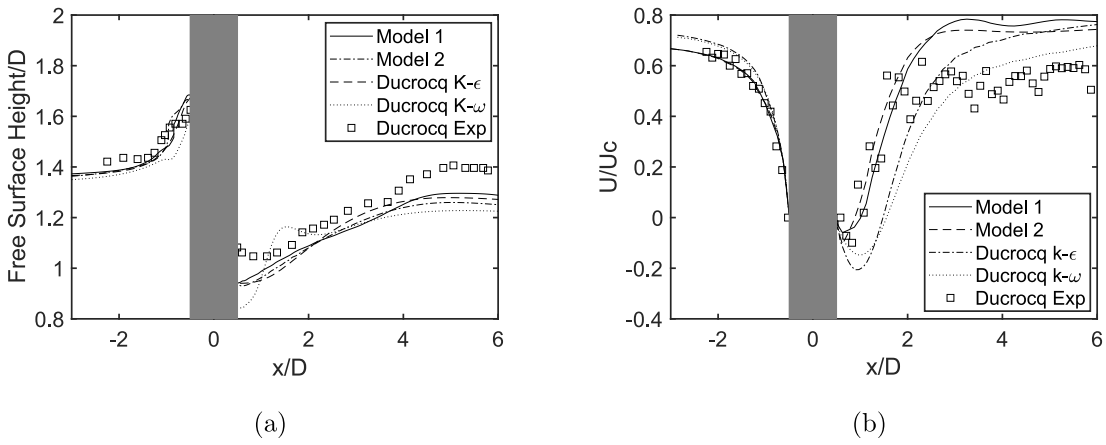

Fig. 6. Results for Flume 2, with the comparison numerical and experimental results are reproduced from [23]. A comparison between (a) the predicted free surface profiles, and (b) free surface velocity sampled along the symmetry plane. See Table 2 for details of Model 1 and 2. Flow direction is from left to right. The pier diameter is $D = 0.04$ m. The critical velocity is related to the Froude number and is given by $U_c = \sqrt{gh_c}$, where the critical depth h_c is based on the total discharge, resulting in $U_c = 0.626$ m/s.

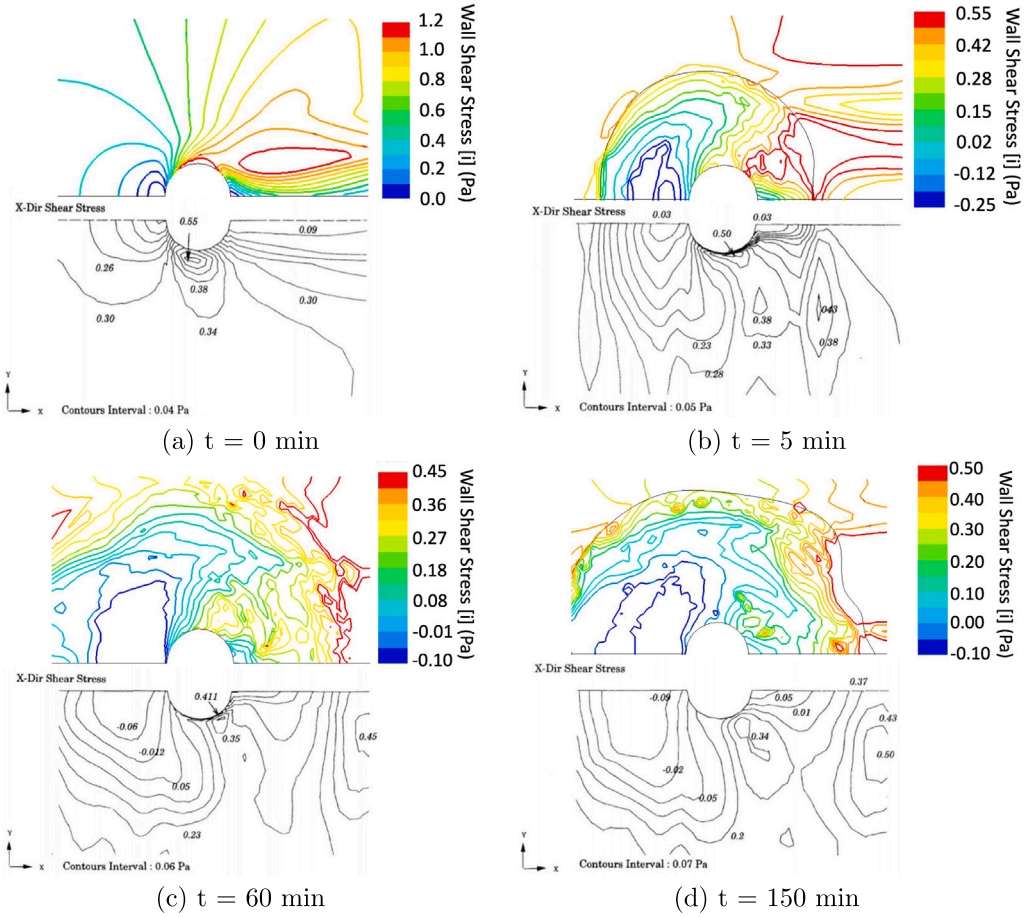

Fig. 7. Validation of bed wall shear stress on temporal scour development. Coloured contours are results obtained by Star-CCM+, and grey scale contours are results reproduced from [33]. The colour levels are set to be the same as black lines. Flow direction is from left to right.

bed as carried out in the present work, and similarly the dynamics at a scour equilibrium necessitates additional modelling results. The review work of [3] has identified details of resuspension, related to eddies in turbulent flow and pore pressure [41–44].

3.1. CFD model and setup validation

The first validation analysis is related to the water-air interface, for which the VoF method was used, and comparison against the

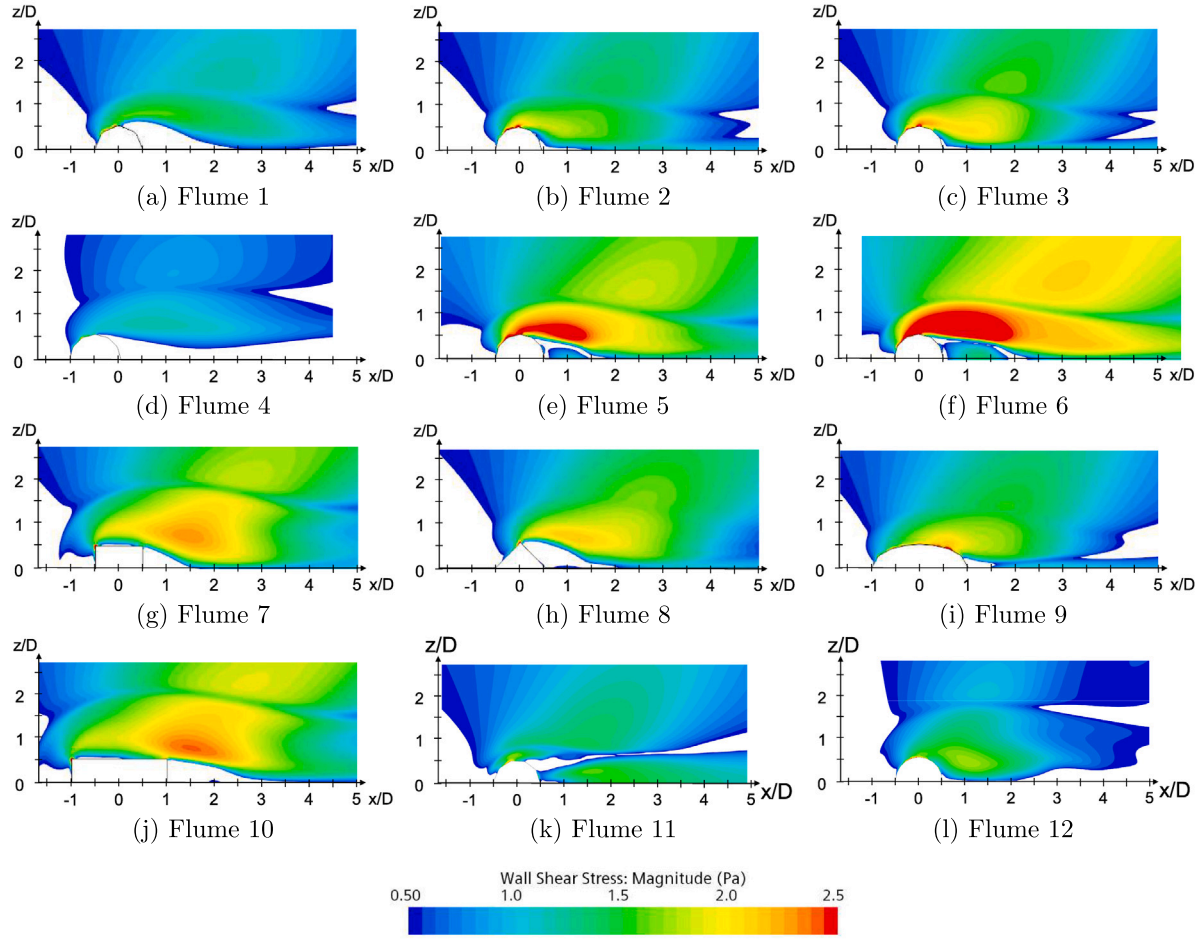

Fig. 8. Bed wall shear stress distributions around piers. Regions where the wall shear stress < 0.5 Pa have been blanked out to provide a visual appreciation of the regions above the critical shear stress for the live bed regime, while the critical shear stress for the clear water regime is $\tau_0 = 1$ Pa.

computational and experimental results of [23] are carried out. The STAR-CCM+ model was found to be sensitive to spatial and temporal discretisation, and a more stringent CFL condition was required for convergence when compared to the OpenFOAM model developed in [23]. Details of the model setup is given in Table 2. Comparing the free surfaces around the pier as shown in Fig. 6, we observe that both the STAR-CCM+ models developed are able to capture the immediate wake region and show good agreement to the results in literature. The free surfaces computed by all the CFD models are smoother than the experimental results, and the surface height in the wake region is underestimated possibly due to numerical damping. From the results of the velocity in the wake region, and includes flow separation due to adverse pressure gradients, we note that the $k-\omega$ model shows a closer agreement to the experimental results than the $k-\epsilon$ model. Therefore, the $k-\omega$ model is seen to be more suitable for the current study.

The second validation analysis is related to the bed wall shear stress. A comparison against the computational results of [33] are carried out, and results for the bed WSS, τ_{bed} are shown in Fig. 7. As scour develops, the WSS decreases since the vorticity generated at the bed surface is reduced and is more effectively transported away from the wall region and into the free-stream flow, with the HV increasing in diameter as is sits inside the scour region and promotes the flow to separate from the bed further upstream from the pier. When the wall shear stress decreases below τ_0, the equilibrium scour depth is effectively reached.

3.2. Parametric study of pier shape and flow conditions

The WSS contour at the flume bed, clipped between 0.5 Pa and 2.5 Pa, are shown in Fig. 8 for all cases listed in Table 1. The area of $\tau > 1$ Pa, indicating the region where scour is highly expected to occur, is also recorded in Table 1.

The isosurface of $\lambda_2 < -50$ provides a clear visualisation of the vortex structure and is presented in Fig. 9. For visualisation clarity, the λ_2 isosurfaces are clipped to show only those in the region $y \leq 0.03$ m for all cases except Flumes 4, 5, 6, in which the cut off heights are 0.03 m, 0.035 m, 0.05 m, respectively. This clipping is done to avoid taking into account of the vortex core of the upward stream while those vortices in the proximity to the river bed are clearly visible. The WSS contour on the flume bed is also shown in Fig. 9. The positions of the HV core lowest point are recorded in Table 1.

3.2.1. Effects of changing diameter of circular pier (Flumes 1, 2, 3)

The effect of varying pier width on the HV is shown in Fig. 9a–c (corresponding to Flume 1–3 in Table 1). The HV core moves both horizontally upstream and vertically away from the flume bed as the pier diameter increases. Additionally, the vortex core enclosed by $\lambda_2 < -50$ also increases in size with the pier diameter increase, highlighting the greater resistance to flow and indicating that a greater portion of the fluid is driven down and around the pier. This increased downwash results in higher values of circulation, which equates to the flux of vorticity, and hence loosely interpreted as a stronger HVs.

From the results presented in Table 1, the HV core position changes modestly with the pier width: a 11.6% increase in normalised HV core y-position corresponds to 33% increase in the pier width from 0.03 m to 0.04 m; a 3% increase in normalised HV core y-position corresponds to 25% increase in the pier width from 0.04 m to 0.05 m.

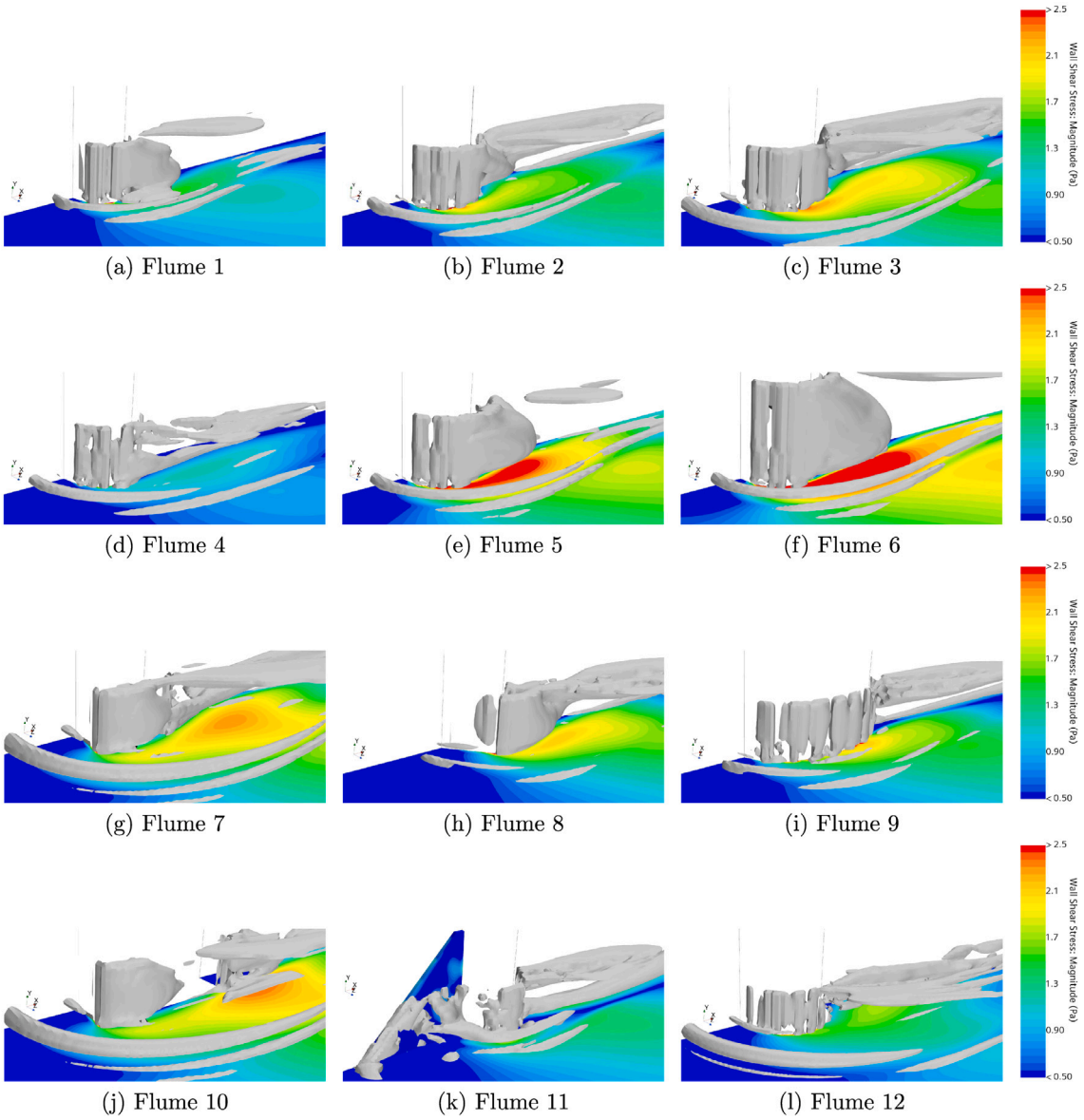

Fig. 9. Vortex structure around piers, visualised using isosurface of $\lambda_2 < -50$ and superimposed on WSS plot. Flow direction is from left to right.

The area of flume bed where the WSS is high, given by $\tau > 1$ Pa, is on the other hand seen to vary noticeably with the pier width, as shown in Fig. 8a–c. The wider piers induce a wider wake region, with the turbulent structures stronger than behind narrower piers, resulting in higher WSS due to higher velocity gradients. From the results presented in Table 1, the area of high WSS increases by 290% when the pier width increases from 0.03 m to 0.04 m, and by 48% when the pier width increases from 0.04 m to 0.05 m. The increase in area with a high WSS is mostly distributed to the side and behind the pier.

3.2.2. *Effects of changing mass flow rate (Flumes 2, 4, 5, 6)*

The effects of varying the MFR on the HV is shown in Fig. 9d–f (Flume 2, 4–6 in Table 1). As the MFR increases the HV core moves vertically away from the flume bed and also horizontally towards the pier, though only modestly. From the results reported in Table 1 we find: a 100% increase in the MFR from 5 kg/s to 10 kg/s does not change the HV core y-position; increasing the MFR from 10 kg/s to 15 kg/s (50%) increases the HV core y-position by 6%; and increasing the MFR from 15 kg/s to 20 kg/s (33%) increases the HV core y-position by 8.6%.

The area of the flume bed where $\tau > 1$ Pa varies greatly as the MFR changes, as shown in Fig. 8d–f, which is again in contrast to the observed changes in HV core position. The high WSS area increases by 1090% when the MFR increases from 5 kg/s to 10 kg/s, by 85.4% from 10 kg/s to 15 kg/s, and by 24.5% from 15 kg/s to 20 kg/s. This suggests that when the MFRs increases, the ability of the flow to carry the sediments increases proportionally more than the increase in proximity of the HV to the flume floor.

3.2.3. *Effects of changing pier shape (Flumes 2, 7, 8, 9, 10)*

Different pier shapes affect the HV y-position by either concentrating or diverting the flow in front of the pier, as shown in Fig. 9g–j (corresponding to Flume 2, 7–10 in Table 1). Among the five shapes tested, the HV y-position ordering from the lowest is: square (45°), elliptical, circular, square, rectangular. For the HV core with greater y-positions, the x-positions are greater as well, indicating a larger HV ahead of the pier. Hence, the sharper the pier leading edge is, the lower HV core y-position because the oncoming flow is more readily diverted to the side of the pier rather than downwards.

The ordering of the extent of high WSS area ($\tau > 1$ Pa), starting from the smallest is given by: circular, elliptical, square (45°), and equal for square and rectangular piers. As the water flows around the pier, it accelerates and brings about a higher WSS. The geometry of the pier influences the rate of flow acceleration, the characteristics of the separated flow and the wake. The square (45°), square and rectangular piers exhibit vortex shedding along the edge extremities due to the discontinuity in curvature, which results in the larger regions of high WSS and wake, unlike the circular and elliptical piers.

Comparing the square (45°) and the elliptical pier, although the sharp edge of the square (45°) pier is more effective at diverting the oncoming flow, the elliptical pier has a smoother transition to the side which accelerates the flow more gradually. As such, the wake region is reduced as is also the area of high WSS.

Comparing the square and rectangular piers, elongating the pier length in the flow direction increases the wake region, due to a greater momentum deficit brought about by the larger surface area of the pier. Nevertheless, only a minor effect on the HV position is observed and the area with high WSS is also unchanged.

3.3. Pier adaptation with debris fin (Flume 11)

Several pier adaptation designs have been devised, each intended to affect specific flow features associated to scour (see Section 1). Debris fins are commonly employed to avoid increased scouring due to debris formation at piers/abutments. Our simulation results show that the debris fin also acts to reduce scour independently of the presence of debris, by disrupting the HV at the pier leading edge. Thus, this suggest that debris fins are functional for reducing scour directly, in addition to avoiding debris formation (which is known to make scour worse). Vortices cannot start or end within a flow, as noted by Helmholtz's second theorem, and indeed they are commonly seen in river flows to start/end on a solid surface (such as the pier or bed) or the free surface, or wrap around to form closed curves (such as vortex rings). Consequently, the presence of the debris fin in effect separates the HV at the pier leading edge, affecting the way it is formed and its strength.

From Fig. 9, we observe that the fin causes leading edge vortex shedding to occur, as well as a vertical vortex running along the juncture of the fin to the pier which develops into a HV-like vortex close to the flume bed. The leading edge vortex shedding runs along the fin, in a similar fashion as on aeroplane swept wings. The vertical vortex arises due to an adverse pressure gradient along the fin as the pier is approached, inducing flow separation and forming a recirculating region which presents itself as a vortex. As this vortex extends towards the bed, it turns effectively parallel to the bed and appears as a HV though of reduced strength due to the reduced flow diverted downwards and consequently a weaker roll-up to form the vortex. The reduced strength of the HV translates to a lower WSS, as evident in Fig. 8k. The area of $\tau > 1$ Pa is 188×10^{-4} m^2, showing 26% reduction when the fin is employed compared to a circular pier with no adaptation (Flume 2). The WSS to the side of the pier is significantly reduced due to slower flow velocity around the pier.

4. Discussion

The results gathered from investigating the effects of changing diameter of the circular pier suggest that the wider the pier is, the greater the extent of scour is also; this relationship relates to the Reynolds number for the pier. This result is primarily supported by the increase in high WSS regions, but also by the increase in size of the HV, see Table 1. Indeed, it is suggested in [45] that an empirical relationship can be obtained between the equilibrium scour depth normalised by pier width, d_s/b, and the pier Reynolds number. Similarly, increasing the MFR also results in an increase in high WSS regions, and consequently the expected extent of scour. However, increasing the MFR increases both the flow depth and the flow velocity, hence the pier Reynolds number and the Froude number. It has also been suggested in [45] that an empirical relationship can be obtained between equilibrium scour normalised by pier width and the Froude number, suggesting that as MFR increases so does the equilibrium scour depth. The review of [3] has identified further works proposing numerous equations relating these measures.

On increasing the diameter of the circular pier or the MFR, the pier Reynolds number increases as does the WSS on the flume bed, however the HV vortex position is seen to vary in different fashion. With an increase in pier diameter or MFR, the HV translates vertically further from the flume bed, but with an increase in pier diameter the HV moves further upstream while with an increase in MFR the HV moves closer to the pier. This difference in horizontal translation behaviour is related to, on the one hand, the resistance to flow when the pier is wider such that there is a larger projected surface area; for this reason, we see an increased flux of water directed downwards below the dividing streamline, which effectively pushes the HV upstream and makes it larger. On the other hand, with the increase in MFR we see a higher fluid momentum which effectively pushes the HV closer to the pier. The vertical translation of the HV is seen to be equally affected by the increase of MFR or pier diameter, since both result in a greater flux of water rolled up into the HV, leading to a larger HV positioned further from the bed. Similar results are reported in [17] in relation to the horizontal position of the HV.

The HV proximity to the floor or pier is seen to vary modestly to changes in Reynolds or Froude numbers, while the effect on high WSS area is more pronounced. The strength of the HV could be described by the circulation, hence the flux of vorticity, and in this comparative analysis we can in general infer that larger vortices can be interpreted as stronger. The distance from the vortex edge, here described by the isosurface of $\lambda_2 = -50$, to the flume bed or pier can be an indicator of vortex strength. These distances and the HV diameter may also be described from the vorticity transport equation (Eq. (10)), in particular the advection and diffusion terms. We may readily note that, while the position and strength of the leading edge HV is relevant, the area of high WSS is prevalently affected by the acceleration around the pier, hence the vortex stretching and vorticity generation. As the HV extends around the pier, it is stretched and in so doing the vorticity increases, with the consequence that the WSS will also increase due to the relation between these properties and the proximity to the flume bed. Indeed, from Eq. (17) we find the relation between the accelerating flow given by a pressure gradient and the opposing viscous forces, and the generation of vorticity on the wall.

From the results of Flumes 2, 7–10, we find the HV position and extent of high WSS area are correlated when consideration of the leading edge blockage are made. The resistance to flow at the pier upstream side affects the extent of downwards directed flow and the resulting HV roll-up. However, it is the strain rate of the flow, which may be observed as the vortex stretching of the HV which occurs as the flow is accelerated around the pier, as well as the extent of the wake due to the displaced flow, which are key factors in the resulting extent of high WSS area. Pier shapes with discontinuity in curvature, which promote flow separation and associated vortex shedding, result in higher strain rates and exhibit larger areas of high WSS on the lateral and downstream sides of the piers.

The results of the parametric study of the pier shapes agrees with the trends reported in the literature [26,46]. A lenticular-shaped pier, as natural extension of the parametric study, has also been proposed as it results in smallest scour depth among other shapes [24]. The lenticular shape indeed presents a sharp leading edge to reduce the blockage to flow with the consequent downwards directed flow, as well as a smooth shape to avoid flow separation and high strain rates as the flow moves around the pier. Frontal areas of piers has been used to obtain a correlation between the scour depth and the pier shape, which the current parametric study results align with the relationship that the blunt-nosed piers generate deeper scours than sharp-nosed piers [24].

Future studies in this area could investigate the fluid mechanics for more pier shapes and/or account for oncoming flows with different angle of attacks, flow rates and depths.

Combining the two measures, the area of $\tau > 1$ Pa is more sensitive to the change in parameters than the HV core position, implying the extent of the scour hole is also more sensitive than the equilibrium scour depth. Increasing the pier width increases both the equilibrium scour depth and the extent of scour. Increasing the MFR increases the extent of scour more than the equilibrium scour depth. The square (45°) pier is expected to cause the smallest scour depth, but the flow separation at the side of the pier would lead to a larger scour hole, compared to circular or elliptical piers. Square or rectangular piers with their flat side facing the oncoming flow would lead to greatest scour depth and extent of scour. For design purposes, metrics for the pier shape accounting for both the pier nose sharpness and the pier geometry smoothness need to be defined. The exact relationship between the pier width, MFR, pier shape, and the HV core position and the area of $\tau > 1$ Pa need to be identified and calibrated to the equilibrium scour depth and scour hole area, and normalised to the pier width or flow depth.

The debris fin is seen to act as an adaptation measure to reduce scour directly, beyond serving to remove debris accumulation (which is known to affect scour, and bridge safety more in general). Indeed, with this adaptation measure we observe the smallest area with high WSS, for the same pier width and river MFR, performing better than any of the different pier designs tested. Similar to the fin, an inclined rod placed upstream to the pier has been shown to suppress the horseshoe vortices [47]. These results suggest that further investigation into adaptation designs involving upwards sweeping structures placed ahead of the pier can serve to reduce scour, and may have additional purposes such as reducing debris and house sensors for monitoring. Future studies may also consider modelling the hydrodynamic effects of debris formation and presence.

5. Conclusion

This paper investigated bridge scour using computational fluid dynamics (CFD) and a robust knowledge of fluid mechanics to analyse the flow field near bridge piers. The horseshoe vortex (HV) core position relative to the bed and the area of wall shear stress (WSS) above a sediment transport threshold of 1 Pa were used as the two indicators to characterise the scour hole. Firstly, the use of CFD for modelling river flow around a bridge pier was validated, demonstrating good accuracy and agreement with the literature in reproducing: (i) WSS in scenarios of varying stages of scour, and (ii) the free surface profile and velocity around the pier. Secondly, the CFD modelling was employed to investigate the effects of different pier widths, river mass flow rates (MFR) and pier shapes. Finally, a debris fin was investigated as an adaptation measure to reduce scour. The mechanisms for scour initiation and progression were discussed in terms of the high WSS and its relation to the HV.

The position of the horseshoe vortex (HV) from the bed and pier was seen to vary modestly, while the extent of high WSS area (where $\tau > 1$ Pa) varied significantly, with the parameter changes of the setup. Increasing the pier width elevates the HV core position and increases the area of $\tau > 1$ Pa around the pier, indicating the equilibrium scour depth and the extent of the scour are both likely to increase. Increasing the flow rate also has similar effect. Piers with sharper leading edge resulted in HV core closer to the flume bed than piers with bluff shape. The extent of the scour depends on the smoothness of the pier geometry, which determines the flow attachment and dynamics of separation at the side of the pier, as well as the strain rate of the fluid as it is accelerated.

The methodology and analysis was then applied to an adapted pier, which has a generic debris fin installed in front of the pier. The HV core had a reduced strength and was only present at the side of the pier. The area of $\tau > 1$ Pa was reduced by 26% compared to the pier before this scour protection: a greater drop than attained with the alternative pier shapes investigated.

The analysis was performed on a single pier, assuming that piers are far apart so that the flow field around each pier does not affect any other. Multiple piers can be investigated in the future to understand possible interactions, how the arrangement of the piers could be optimised to reduce scouring, and the effectiveness of proposed adaptations. Additionally, different flow directions should be considered, in order to observe the effects of angle of attack on the debris fin and identify the range where the fin can act successfully. Alternative designs, such as the inclined rod studies in [47] should be further investigated, as well as other possible designs.

While we have not discussed monitoring techniques, a readily available measurement is that of pressure sensors. Some attempt has been made to use a map of the pressure on the wall to interpret the flow around a cylinder on a wall [17,48], however both these studies were apparently not carried out with scour in mind. It would be of interest to relate the HV position, the WSS and the vortex stretching in terms of a pressure field, which has been discussed here in terms of vorticity generation only.

This study emphasises the successful use of CFD to investigate scour dynamics around bridge piers and investigate adaptation (retrofitting) options for the piers. The presented method could be applied to a wider range of onward flows, pier types and adaptation choices. Moreover, despite being demonstrated for bridges, it could also be adopted and adapted for other structures suffering scour formation (e.g. off-shore wind turbines, river embankments or pipelines). Results are encouraging for asset owners or operator organisations who are targeting safer and more resilient structures.

CRediT authorship contribution statement

Xin L. Tu: Conceptualization, Investigation, Methodology, Validation, Visualization, Writing – original draft, Writing – review & editing, Data curation. **Alberto M. Gambaruto:** Conceptualization, Investigation, Methodology, Project administration, Resources, Supervision, Writing – original draft, Writing – review & editing. **Richard Newell:** Writing – original draft, Conceptualization. **Maria Pregnolato:** Investigation, Methodology, Writing – original draft.

Declaration of competing interest

The authors declare the following financial interests/personal relationships which may be considered as potential competing interests: Maria Pregnolato reports financial support was provided by Engineering and Physical Sciences Research Council. Xin L. Tu reports financial support was provided by EPSRC Centre for Doctoral Training in Future Innovation in Non-destructive Evaluation (FIND-CDT). If there are other authors, they declare that they have no known competing financial interests or personal relationships that could have appeared to influence the work reported in this paper.

Acknowledgements

MP was supported by the Engineering and Physical Sciences Research Council (ESPRC) LWEC (Living With Environmental Change) Fellowship (EP/R00742X/2). XLT is funded by EPSRC FIND-CDT, United Kingdom, grant number: EP/S023275/1.

References

[1] Arneson L, Zevenbergen L, Lagasse P, Clopper P. Evaluating Scour at Bridges. 5th ed.. 2012, URL https://www.fhwa.dot.gov/engineering/hydraulics/pubs/hif12003.pdf.

[2] Wardhana K, Hadipriono FC. Analysis of recent bridge failures in the United States. J Perform Constr Facil 2003;17:144–50. http://dx.doi.org/10.1061/(ASCE)0887-3828(2003)17:3(144).

[3] Gazi AH, Afzal MS. A review on hydrodynamics of horseshoe vortex at a vertical cylinder mounted on a flat bed and its implication to scour at a cylinder. Acta Geophys 2020;68:861–75.

[4] Wang C, Yu X, Liang F. A review of bridge scour: mechanism, estimation, monitoring and countermeasures. Nat Hazards 2017;87:1881–906.

[5] Pizarro A, Manfreda S, Tubaldi E. The science behind scour at bridge foundations: A review. Water 2020;12(2):374.

[6] Tubaldi E, White CJ, Patelli E, Mitoulis SA, De Almeida G, Brown J, Cranston M, Hardman M, Koursari E, Lamb R, et al. Invited perspectives: Challenges and future directions in improving bridge flood resilience. Nat Hazards Earth Syst Sci 2022;22(3):795–812.

[7] Kirby A, Roca M, Kitchen A, Escarameia M, Chesterton O. 2nd ed.. Manual on scour at bridges and other hydraulic structures, vol. C742, London: CIRIA; 2015.

[8] Pregnolato M, Winter A, Mascarenas D, Sen A, Bates P, Motley M. Assessing flooding impact to riverine bridges: an integrated analysis. Nat Hazards Earth Syst Sci 2020;1–18. http://dx.doi.org/10.5194/nhess-2020-375.

[9] Mathews R, Hardman M. Lessons learnt from the december 2015 flood event in cumbria, UK. Proc Inst Civ Eng Forensic Eng 2017;170(4):165–78.

[10] Dikanski H, Imam B, Hagen-Zanker A. Effects of uncertain asset stock data on the assessment of climate change risks: A case study of bridge scour in the UK. Struct Saf 2018;71:1–12.

[11] Pagliara S, Carnacina I. Influence of large woody debris on sediment scour at bridge piers. Int J Sediment Res 2011;26(2):121–36.

[12] Jannaty M, Eghbalzadeh A, Hosseini S. Using field data to evaluate the complex bridge piers scour methods. Can J Civil Eng 2016;43(3):218–25.

[13] Wipf TJ, Phares BM, Dahlberg JM, et al. Debris mitigation methods for bridge piers. Tech. rep, Iowa State University. Institute for Transportation; 2012.

[14] Bradley J, Richards D, Bahner C, et al. Debris control structures-evaluation and countermeasures, third edition: hydraulic engineering circular 9. Tech. rep, United States. Federal Highway Administration. Office of Bridge Technology; 2005.

[15] Unger J, Hager W. Down-flow and horseshoe vortex characteristics of sediment embedded bridge piers. Exp Fluids 2007;42:1–19. http://dx.doi.org/10.1007/s00348-006-0209-7.

[16] Mohammed TA, Noor MJMM, Ghazali AH, Yusuf B, Saed K. Physical modeling of local scouring around bridge piers in erodable bed. J King Saud Univ, Eng Sci 2007;19(2):195–206. http://dx.doi.org/10.1016/S1018-3639(18)30947-4.

[17] Baker C. The laminar horseshoe vortex. J Fluid Mech 1979;95(2):347–67.

[18] Sumer BM, Christiansen N, Fredsøe J. The horseshoe vortex and vortex shedding around a vertical wall-mounted cylinder exposed to waves. J Fluid Mech 1997;332:41–70.

[19] Fakhimjoo MS, Ardeshir A, Behzadian K, Karami H. Experimental investigation and flow analysis of clear-water scour around pier and abutment in proximity. Water Sci Eng 2023;16(1):94–105. http://dx.doi.org/10.1016/j.wse.2022.12.001.

[20] Chase KJ, Holnbeck SR. Evaluation of pier-scour equations for coarse-bed streams. 2004, http://dx.doi.org/10.3133/SIR20045111.

[21] Brunner G. HEC-RAS, river analysis system hydraulic reference manual. US Army Corps of Engineers Hydrauluc Engineering Center (HEC); 2020, p. 290–3.

[22] Xiong W, Cai C, Kong B, Kong X. CFD simulations and analyses for bridge-scour development using a dynamic-mesh updating technique. J Comput Civ Eng 2016;30(1):04014121.

[23] Ducrocq T, Cassan L, Chorda J, Roux H. Flow and drag force around a free surface piercing cylinder for environmental applications. Environ Fluid Mech 2017;17:629–45. http://dx.doi.org/10.1007/s10652-016-9505-9.

[24] Vijayasree B, Eldho T, Mazumder B, Ahmad N. Influence of bridge pier shape on flow field and scour geometry. Int J River Basin Manag 2019;17(1):109–29.

[25] Jalal HK, Hassan WH. Effect of bridge pier shape on depth of scour. In: IOP conference series: materials science and engineering. vol. 671, IOP Publishing; 2020, 012001.

[26] Fael C, Lança R, Cardoso A. Effect of pier shape and pier alignment on the equilibrium scour depth at single piers. Int J Sediment Res 2016;31(3):244–50.

[27] SIEMENS. Simcenter STAR-CCM+ documentation, 2020.3.1. 2020, URL https://plm.sw.siemens.com/en-US/simcenter/fluids-thermal-simulation/star-ccm/.

[28] Gazi A, Afzal MS. A review on hydrodynamics of horseshoe vortex at a vertical cylinder mounted on a flat bed and its implication to scour at a cylinder. Acta Geophys 2020;68. http://dx.doi.org/10.1007/s11600-020-00439-8.

[29] Hunt J, Wray A, Moin P. Eddies, streams, and convergence zones in turbulent flows. Stud Turbul Using Numer Simul Databases 1988;-1:193–208.

[30] Jeong J, Hussain F. On the identification of a vortex. J Fluid Mech 1995;285:69–94. http://dx.doi.org/10.1017/S0022112095000462.

[31] Nasif G, Balachandar R, Barron RM. International journal of multiphase flow mean characteristics of fluid structures in shallow-wake flows. Int J Multiph Flow 2016;82:74–85. http://dx.doi.org/10.1016/j.ijmultiphaseflow.2016.03.001.

[32] Guo J. Empirical model for shields diagram and its applications. J Hydraul Eng 2020;146(6):04020038. http://dx.doi.org/10.1061/(ASCE)HY.1943-7900.0001739.

[33] Kamil HA, Othman K. Simulation of flow around piers. J Hydraul Res 2002;4(2):161–74. http://dx.doi.org/10.1080/00221680209499859.

[34] Panton RL. Incompressible flow. John Wiley & Sons; 2013.

[35] Lighthill M. Introduction: Boundary layer theory. Laminar Bound Layer 1963;46—-109.

[36] Cottet G-H, Koumoutsakos PD, et al. Vortex methods: theory and practice. vol. 8, Cambridge university press Cambridge; 2000.

[37] Baker C. The turbulent horseshoe vortex. J Wind Eng Ind Aerodyn 1980;6(1–2):9–23.

[38] Sahin B, Ozturk NA, Akilli H. Horseshoe vortex system in the vicinity of the vertical cylinder mounted on a flat plate. Flow Meas Instrum 2007;18(2):57–68.

[39] Melville BW, Chiew Y-M. Time scale for local scour at bridge piers. J Hydraul Eng 1999;125(1):59–65.

[40] Shahhosseini M, Yu G. Experimental study on the effects of pier shape and skew angle on pier scour. In: Journal of physics: conference series. vol. 1300, IOP Publishing; 2019, 012031.

[41] Gioia G, Bombardelli FA. Localized turbulent flows on scouring granular beds. Phys Rev Lett 2005;95(1):014501.

[42] Engelund F, Fredsøe J. Hydraulic theory of alluvial rivers. In: CHOW VT, editor. In: Advances in hydroscience, vol. 13, Elsevier; 1982, p. 187–215. http://dx.doi.org/10.1016/B978-0-12-021813-4.50009-3, URL https://www.sciencedirect.com/science/article/pii/B9780120218134500093.

[43] Dey S, Sarkar S, Solari L. Near-bed turbulence characteristics at the entrainment threshold of sediment beds. J Hydraul Eng 2011;137(9):945–58.

[44] Tonkin S, Yeh H, Kato F, Sato S. Tsunami scour around a cylinder. J Fluid Mech 2003;496:165–92.

[45] Mohammed TA, Noor MJMM, Ghazali AH, Yusuf B, Saed K. Physical modeling of local scouring around bridge piers in erodable bed. J King Saud Univ, Eng Sci 2007;19(2):195–206.

[46] Farooq R, Ghumman AR. Impact assessment of pier shape and modifications on scouring around bridge pier. Water 2019;11(9):1761.

[47] Wang J, Bi W, Wei Q. Effects of an upstream inclined rod on the circular cylinder–flat plate junction flow. Exp Fluids 2009;46:1093–104.

[48] Tobak M, Coon M. Topology of pressure surfaces in three-dimensional separated flows. In: 34th aerospace sciences meeting and exhibit. 1990, p. 319.